TOPMELT 1.0: A topography-based distribution function approach to snowmelt simulation for hydrological modelling at basin scale

Mattia Zaramella[1], Marco Borga[1], Davide Zoccatelli[1], and Luca Carturan[1,2]

[1]Department of Land, Environment, Agriculture and Forestry, University of Padua, Padova, 35020, Italy
[2]Department of Geosciences, University of Padua, Padova, 35131, Italy

Correspondence: Mattia Zaramella (mattia.zaramella@unipd.it)

Abstract. Enhanced temperature-index distributed models for snowpack simulation, incorporating air temperature and a term for clear sky potential solar radiation, are increasingly used to simulate the spatial variability of the snow water equivalent. This paper presents a new snowpack model (termed TOPMELT) which integrates an enhanced temperature index model into a lumped basin scale hydrological model by exploiting a statistical representation of the distribution of clear sky potential solar radiation. This is obtained by discretising the full spatial distribution of clear sky potential solar radiation into a number of radiation classes. The computation required to generate a spatially distributed water equivalent reduces to a single calculation for each radiation class. This turn into a potentially significant advantage when parameter sensitivity and uncertainty estimation procedures are carried out. The model includes a routine, which accounts for the variability of clear sky radiation distributions with time, ensuring a consistent temporal simulation of the snow mass balance. Thus, the model resembles a classical temperature-index model when only one radiation class for each elevation band is used, whereas it approximates a fully distributed model with increasing the number of the radiation classes (and correspondingly decreasing the area corresponding to each class). TOPMELT is applied over the Aurino basin at S. Giorgio, a 614 km[2] catchment in the Upper Adige river basin (Eastern Alps, Italy) to examine the sensitivity of the snowpack model results to the temporal and spatial aggregation of the radiation fluxes.

1 Introduction

Seasonal snow cover is an important storage and source of melt water for human use, irrigation and hydropower production in many regions of the world. On the other hand, snow cover and melt water can be a cause of disastrous natural hazards, such as floods and avalanches. Additionally, snow cover is a key factor in the weather and climate system, both regionally and globally (Armstrong et al., 2008). Owing to the society's strong need for updated information on snow conditions, snow accumulation and melt, models have been developed with a wide range of features. Approaches for snowpack computation range from empirical models (e.g. simple temperature index models) to more-sophisticated physically based energy-balance models (Avanzi et al., 2016; Magnusson et al., 2015; Essery et al., 2013; Vionnet et al., 2012). Temperature-index models require only temperature as input and are based on the assumption of a linear relationship between this variable and melt rates, whereas energy-balance models are based on the computation of all relevant energy fluxes at the snowpack surface, and thus

require extrapolation of numerous meteorological and surface input variables at local scale (Jóhannesson et al., 1995; Cazorzi and Dalla Fontana, 1996; Hock, 1999; Hock and Holmgren, 2005; Anslow et al., 2008; Formetta et al., 2014). Advances over the simple dependence of melt on air temperature by addition of radiation terms have been suggested in the last decades (e.g. Hock, 1999; Pellicciotti et al., 2005, Carturan et al., 2012), and are termed enhanced temperature-index models (ETI) here. In

5 contrast to simple temperature-index models, where melt varies in space only as a function of elevation (given by temperature lapse rates), ETI models includes a term for clear sky potential solar radiation. This term accounts for topographic effects (e.g. aspect, slope and shading) on the spatial distribution of melt, without the need for additional meteorological variables (e.g. global radiation and cloud data). ETI models have been found to provide a better representation of the spatial and temporal variability of melt controlled by solar radiation, when compared with simple temperature index models, as reported by a

10 number of authors (Cazorzi and Dalla Fontana, 1996; Hock, 1999; Pellicciotti et al., 2005; Carenzo et al., 2009 among others). Some of these approaches also better cope with the physical character of the melt process and provide a promising approach to modelling the snowpack at the catchment scale with fewer input data than energy-balance models, but allowing better model parameter transferability than standard temperature-index models (Carenzo et al., 2009).

In spite of their improved accuracy compared to simpler approaches, ETI models have been so far not integrated within

15 lumped, basin-scale hydrological modelling schemes, which are still frequently used to model sparsely gauged mountainous catchments. In a few cases, lumped models have been proposed which incorporate a spatial discretization in elevation and aspect classes to represent the effect of different expositions on snow melt and adjusting accordingly the model snowpack parameter (Konz and Seibert, 2010; Abudu et al., 2016). In other cases, a mean value of radiation has been used over the basin area in the same elevation band, modifying accordingly the melt parameters (Li and Williams, 2008). However, these types of

20 tessellation have no allowance for representing the actual variations of radiation distribution over space and time.

This work describes a novel snowpack model (termed TOPMELT herewith), which integrates the ETI snowpack method originally developed in a spatially distributed way by Cazorzi and Dalla Fontana (1996) within a lumped basin-scale hydrological model. In the model developed by Cazorzi and Dalla Fontana (1996), local snowmelt is computed by using a combined melt factor which is multiplied by a radiation index and positive air temperature. With TOPMELT, pixels with similar radiation

25 index and air temperature are identified by subdividing basin elevation bands into a number of radiation index classes. Then, the snowpack modelling is carried out for each class of radiation index and for each elevation band. This ensures to achieve the significant computational efficiency, which characterizes the temperature index models, allowing at the same time the higher accuracy of ETI models. This is a potentially significant advantage when parameter sensitivity and uncertainty estimation procedures are carried out.

30 As the spatial distribution of clear sky solar radiation changes with time, a radiation class computed at two different times corresponds to two different areas of the elevation band. This means that a pixel belonging to a certain class at a given time, will belong to a different class at another time. TOPMELT incorporates a time-integration routine, which accounts for the temporal variability of the radiation index distribution, ensuring a consistent temporal simulation of the snowpack. Thus, TOPMELT permits full implementation of the ETI snowpack method taking into account the seasonal evolution of the spatial distribution

35 of solar radiation. Moreover, it provides a spatially continuous mapping of simulated snow water equivalent, in spite of the

computationally-efficient lumped representation of basin-scale snowpack modelling. Depending on the number of radiation classes which are used in the model, the snowpack model makes use of solar radiation values which are spatially averaged over different areas. Effectively, the model resembles a classical temperature-index model when only one radiation class for each elevation band is used, whereas it approximates a fully distributed model with increasing the number of the radiation classes

5   (and correspondingly decreasing the area corresponding to each class).

The balance between computational efficiency and model accuracy is not only affected by the spatial averaging of the radiation values. The model permits also the use of temporally averaged values of solar radiation values. This means that a time-averaged solar radiation distribution is used over a given temporal interval (termed here updating interval), before substituting it with a new averaged distribution. With decreasing the updating interval, the accuracy of the model increases at

10   the expenses of the computational efficiency.

This paper describes in detail the structure of TOPMELT and of the time-integration routine. The integration of TOPMELT within the ICHYMOD hydrological model is also illustrated. Finally, results are reported from the application of TOPMELT over the 614 km^2 Aurino basin at S. Giorgio in the Upper Adige river system (Eastern Italian Alps). The case study is exploited to i) examine the sensitivity of the snowpack model results to the temporal and spatial aggregation of the radiation fluxes, and

15   ii) to identify suitable spatial and temporal aggregation intervals for model simulation. The sensitivity analysis is performed on modelled snowpack in terms of snow water equivalent, comparing the output from simulations performed at different aggregation intervals with a reference represented by the finest aggregation levels.

2   TOPMELT structure

In TOPMELT, the basin area is subdivided into elevation bands to account for air temperature variability with elevation. Then,

20   each elevation band is subdivided into a number of radiation classes. This is carried out by dividing each elevation band into a number n_c of equally distributed radiation classes, where the *i-th* class contains the band sub-area corresponding to the *i-th* percentile of the incident radiation energy. Therefore, the model spatial domain is represented by n_b elevation bands and by n_c radiation classes for each elevation band. Each one of the $n_b \times n_c$ model cells is characterised by a fraction of glacier area and of debris-covered glacier area. The spatial subdivisions controls the balance between computational efficiency and model

25   accuracy in the snowpack model.

The following sections describe the main modules of the model, where an hourly temporal interval is used for model computations.

2.1   Clear sky potential radiation computation and derivation of radiation distributions

Clear sky short wave solar radiation [Wm^{-2}] is computed at each element of the Digital Terrain Model (DTM) by taking into

30   account shadow and complex topography. The model estimates the apparent sun motion (Swift , 1976; Lee, 1978; Oke, 1992) and computes the intersection of radiation with topography (Dubayah et al., 1990; Ranzi and Rosso, 1991). Diffuse radiation is computed by accounting for self-shading (by slope and aspect) and occlusions produced by the visible horizon. Clear sky

solar radiation is computed at each DTM grid at any time instant. Since the model uses radiation values averaged over a given time interval, maps of potential radiation averaged over time are also computed. The spatial distribution of time-averaged clear sky solar radiation are computed over each elevation band, and n_c equally distributed radiation classes are identified. For each radiation class, the mean clear sky radiation value is computed (termed Radiation Index RI herewith) and used in the snowmelt

5   computation.

2.2 Computation of precipitation amount and phase

Snow accumulation is computed starting from the estimation of precipitation and air temperature over each elevation band. Air temperature and precipitation data are acquired at hourly time interval from the available weather stations. A single temperature lapse rate is estimated based on temperature data. To account for gage catch deficiencies that occur during periods of snow,

10   precipitation data are corrected with a Snow Correction Factor (SCF). This is a multiplier of the precipitation data which is applied when station temperature is lower than a threshold temperature T_c.

Mean basin areal precipitation values are obtained by using techniques ranging from Thiessen's polygons to multi-quadratic and Kriging methods. Finally, the basin precipitation value P_{basin} is obtained by applying a non-dimensional Precipitation Correction Factor (PCF) to account for poor spatial representativeness of rain-gauge stations. The precipitation value at the *i-th*

15   elevation band P_i [mm h^{-1}] is obtained by using a vertical precipitation gradient, accounting for increased precipitation over elevation. Based on results from Tuo et al. (2016), this is obtained by means of a precipitation gradient G [% km^{-1}], as follows:

$$P_i = P_{basin} \cdot \left(1 + G \cdot \frac{H_i - H_{ref}}{1000} \right) \tag{1}$$

where H_i and H_{ref} [m a.s.l.] are the mean altitude of the *i-th* elevation band and of the basin respectively. Eq. 1 is applied in

20   a way to modify only the distribution of precipitation across the elevation bands without altering the value of P_{basin}.

A mean value of air temperature T_i over the *i-th* elevation band is obtained by using the vertical temperature lapse rate. Estimation of precipitation phase (solid or liquid) is therefore performed over each elevation band, according to the temperature lapse rate and the threshold temperature T_c.

2.3 Computation of snow and ice melt

25   For the generic model cell represented by the *i-th* elevation band and the *j-th* radiation class, snow melt rate $F_{i,j}(t)$ [mm h^{-1}] at time t, is computed taking into account air temperature, clear sky radiation and albedo. During day hours, the snowmelt is given by:

$$F_{i,j}(t) = CMF \cdot RI_{i,j}(t) \cdot (1 - alb_i(t)) \cdot \max[0, (T_i(t) - T_b)] \tag{2}$$

where: $T_i(t)$ is the elevation band temperature, $RI_{i,j}(t)$ [J^{-2}h^{-1}] is the cell radiation index, CMF [mm°C^{-1}J^{-1}m^2] is the combined

30   melt factor, accounting for both thermal and radiative effects; $ALB_i(t)$ [-] is the albedo of snow, $T_b = 0$ °C is a threshold base

temperature. Snow albedo is computed for each elevation band based on Brock et al. (2000):

$$ALB_i(t) = ALBS - \beta_2 \cdot \left[\log_{10} \sum_k T_i(t_k) \right] \tag{3}$$

where $ALBS$ [-] is the fresh snow albedo, β_2 [-] is a dimensionless parameter, $\sum_k T_i(t_k)$ [°C] is the sum of the positive hourly temperatures exceeding the threshold base temperature T_b since the last snowfall until the current time t.

5   During night hours, snow melt is simulated by accounting only for air temperature, as follows:

$$F_{i,j}(t) = NMF \cdot \max\left[0, (T_i(t) - T_b)\right] \tag{4}$$

where NMF [mm h^{-1} °C^{-1}] is the night melt factor.

rain-on-snow conditions, melting is computed depending on air temperature and on the energy provided by rain:

$$F_{i,j}(t) = \left[RMF + \frac{P_{i,j}(t)}{cost} \right] \cdot \max\left[0, (T_i(t) - T_b)\right] \tag{5}$$

where RMF [mm h^{-1} °C^{-1}] is the rain melt factor and cost [°C^{-1}] is a parameter accounting for the influence of rain on snowmelt (Carturan et al., 2012). For each model cell, the snow water equivalent ($WE_{i,j}$ [mm]) is updated by accounting for snow accumulation, rain-on-snow, melt and freezing water. Water due to snowmelt or rainfall is first retained in the snowpack as interstitial water termed Liquid Water $LIQW_{i,j}$ [mm]. When Liquid Water exceeds a water holding capacity of the snowpack (termed LWT), this propagates through the snowpack at a rate $DYTIME$ [m h^{-1}], to form net water flow at the snowpack

15   base.

When air temperature is less than the threshold base temperature, part of the liquid water refreezes and $LIQW_{i,j}$ is reduced and added to the snowpack through a freezing rate, termed ICE [mm h^{-1}]. This is computed as:

$$ICE_i(t) = REFRZ \cdot \min\left[0, (T_b - T_i(t))\right] \tag{6}$$

where T_b is the threshold base temperature (Eq. 2) and $REFRZ$ [mm °C^{-1} h^{-1}] is the freezing factor. When $WE_{i,j}$ is less

20   than a threshold (termed $WETH$), ice melt starts. This is computed similarly to snow (Eq. 2), but where the snow albedo is replaced by a constant glacial albedo, $ALBG$ [-], as follows:

$$F_{i,j}(t) = CMF \cdot RI_{i,j} \cdot (1 - ALBG) \cdot \max\left[0, (T_i(t) - T_b)\right] \tag{7}$$

In case of debris cover, ice melt is reduced accordingly with the following relationship (Östrem, 1959):

$$F_{i,)}(t) = CMF \cdot RI_{i,j} \cdot (1 - ALBG) \cdot T_i(t) \cdot \left[1 - \frac{A^d_{i,j}}{A^g_{i,j}} \cdot \left(1 - e^{-\Gamma}\right) \right] \cdot \max\left[0, (T_i(t) - T_b)\right] \tag{8}$$

25   where Γ [-] is a non-dimensional parameter accounting for the geometry of the debris cover (thickness and mean slope); $A^d_{i,j}$ is the debris-covered surface of the glacial area $A^g_{i,j}$ relative to the *j-th* radiation class and *i-th* elevation band. During rainfalls or night hours, glacier melt is computed by means of Eq. 4 and Eq. 5 respectively.
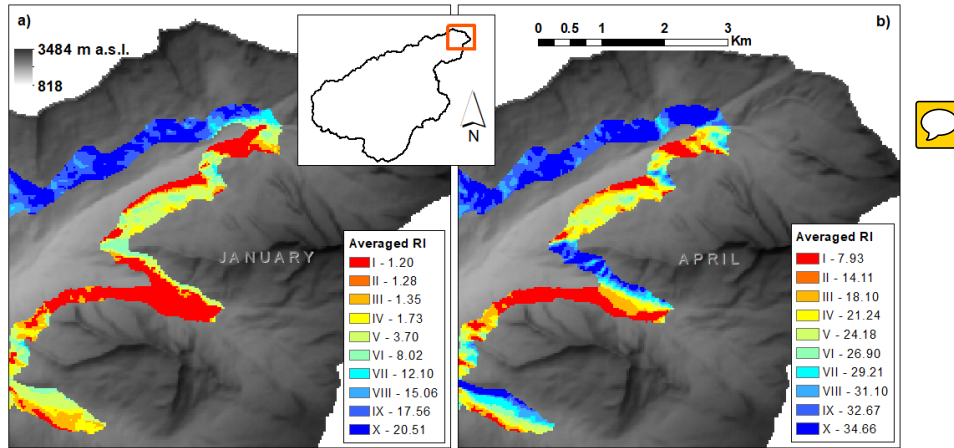
Figure 1. Comparison between radiation index distribution over the 2000-2200 m elevation band of the Aurino basin for a) January 1st and b) April 1st (ten classes subdivision). The figures show the north-eastern portion of the basin and report the average radiation index [J m^{-2}h^{-1}], with the corresponding radiation class identified by a roman number.

2.4 Updating the Radiation Index distribution: the time-integration routine

As reported in the previous sections, the spatial distribution of clear sky solar radiation changes with time, based both on astronomic variation of the radiation flux and its interaction with a complex topography. This implies that the statistical distribution of the radiation index over each elevation band will be also modified and should be updated. In general, a radiation class computed at two different times covers two different areas of the elevation band. This means that a pixel belonging to a certain class at a given time, will belong to a different class at another time. Figure 1 shows two different maps of RI, (representing January 1 and April 1, from an elevation band ranging from 2000 to 2200 m a.s.l., taken from the basin selected for the case study of this work. The radiation index is distributed using ten equally-distributed classes. While the radiation index varies from 1.2 to 20.5 MJ m^{-2}h^{-1} in January, it ranges from 7.9 and 34.7 MJ m^{-2}h^{-1} in April. However, differences are not restricted to the magnitude of the index. Despite each class has the same area within the elevation band, their spatial distribution changes from one map to the other. Examination of the figures shows that a number of pixel belonging to Class V in January are included in Class IX in April. Since the two snowpack state variables, WE and $LIQW$, are computed at the model cell level, pixel transition from a given cell to another must be accounted for, whenever the radiation index distribution is updated with time (termed switch date here). To account for pixel transition through classes, TOPMELT implements an adjusting procedure for model state variables. The procedure is here described applied to the arbitrary cell state variable $X_{i,j}$, corresponding to the *i-th* elevation band and the *j-th* radiation class of the basin. When updating from one radiation index map to another, pixels from a certain class can, in principle, move to all other classes, and pixels from other classes can conversely move to that class. The $X_{i,j}$ variable, which corresponds to certain model cell, should be updated accordingly. Therefore, a 2-D array accounting for

pixels transition and the associated variables among classes is defined, namely the transition matrix $\mathbf{M}_i$ of the *i-th* elevation band.

The transition matrix is $n_c \times n_c$ sized and is computed for each elevation band and is unique for each switch date of the radiation index maps. The element $M_{i,j,k}$ of the matrix represents the number of pixels moving at a switch date from the *j-th*

5   source class to the *k-th* destination class, within a given elevation band i. $M_{i,j,j}$ is the diagonal element of $\mathbf{M}_i$, representing the pixels that did not move from the source radiation class. Provided that the total number of pixels belonging to a class must remain constant, a property of the transition matrix is that the sum of the elements along the *i-th* row is equal to the sum of the elements of the *j-th* column (i.e. the number of pixels leaving a class is replaced by an equivalent number of pixels migrating from other classes):

10
$$\sum_{h=1}^{n_c} M_{i,j,h} = \sum_{h=1}^{n_c} M_{i,h,j} = N_{i,j} \tag{9}$$

where $N_{i,j}$ is the number of pixels in the *j-th* radiation class within the *i-th* elevation band. When TOPMELT switches from one radiation index map to another, the cell state variable $X_{i,j}$ in the new model cell will be the sum of the pixel contribution from other classes and of the pixels remaining in the source class, where the number of incoming or remaining pixels is weighted with respect to the total number of pixels of the source class. Therefore, $X_{i,j}$ is corrected through a matrix $\mathbf{C}_i$ of correction

15   coefficients, relative to the *i-th* elevation band, which can be derived from $\mathbf{M}_i$ through the following relation:

$$C_{i,j,k} = \frac{M_{i,j,k}}{N_{i,j}} \tag{10}$$

Follows from Eq. 9 and Eq. 10 that the sum of each line or column of the correction factors matrix $\mathbf{C}_i$ must be equal to 1:

$$\sum_{j=1}^{n_c} C_{i,j,k} = \sum_{j=1}^{n_c} \frac{M_{i,j,k}}{N_{i,j}} = 1 \tag{11}$$

The coefficient $C_{i,j,k}$ represents the correction factor for the state variable $X_{i,j}$ that must be redistributed among the other

20   classes through the updating process, within the *i-th* elevation band. With the updating, if $X_{i,j}$ is the source class variable band and $X_{i,j}$ its transformed (i.e. destination), the class variable correction is computed through the following:

$$\widehat{\mathbf{X}}_i = \mathbf{C}_i \cdot \mathbf{X}_i \tag{12}$$

or through the equivalent forms:

$$\begin{bmatrix} \widehat{X}_{i,1} \\ \widehat{X}_{i,2} \\ \vdots \\ \widehat{X}_{i,n_c} \end{bmatrix} = \begin{bmatrix} C_{i,1,1} & C_{i,1,2} & \cdots & C_{i,1,n_c} \\ C_{i,2,1} & C_{i,2,2} & \cdots & C_{i,2,n_c} \\ \vdots & \vdots & \ddots & \vdots \\ C_{i,n_c,1} & C_{i,n_c,2} & \cdots & C_{i,n_c,n_c} \end{bmatrix} \cdot \begin{bmatrix} X_{i,1} \\ X_{i,2} \\ \vdots \\ X_{i,n_c} \end{bmatrix} \tag{13}$$

25   and

$$\widehat{X}_{i,j} = \sum_{k=1}^{n_c} C_{i,j,k} X_{i,k} \tag{14}$$

Eq. 14 represents the weighted sum of $X_{i,k}$ pixels that moved from the n_c source classes to destination *k-th* class. Since the correction factors matrix $\mathbf{C}_i$ can be computed once for all, the model computational efficiency is preserved.

To exemplify the computational flow and its constraints, the example of the water equivalent WE state variable is reported here. At a given radiation index switch, $WE_{i,j}$, will be transferred within the *i-th* elevation band across different classes transforming into $\widehat{WE}_{i,j}$, for $j = 1, n_c$. The total volume of snow at a given elevation band i of the destination distribution is:

$$\widehat{V}_i^{WE} = \sum_{j=1}^{n_c} \left(\widehat{WE}_{i,j} N_{i,j} A_p \right) \tag{15}$$

where A_p is the pixel size. Combining Eq. 14 and Eq. 15, and provided that the number of pixels is the same for each class of the *i-th* elevation band ($N_{i,j} = N_i$ for $j = 1, n_c$):

$$\widehat{V}_i^{WE} = N_i A_p \sum_{j=1}^{n_c} \left[\sum_{k=1}^{n_c} (C_{i,j,k} WE_{i,k}) \right] = N_i A_p \sum_{k=1}^{n_c} \left(WE_{i,k} \sum_{j=1}^{n_c} C_{i,j,k} \right) \tag{16}$$

Eq. 11 plus Eq. 16 yield that the transformed WE volume is equal to original volume:

$$\widehat{V}_i^{WE} = N_i A_p \sum_{k=1}^{n_c} WE_{i,k} = V_i^{WE} \tag{17}$$

Therefore, Eq. 11 is a constraint that holds conservation of WE through the updating process.

2.5 Representation of the water equivalent distribution and snow cover

The model allows to provide the representation of spatially continuous water equivalent maps (as well as any other model cell variable) at a given time. This is carried by exploiting a routine which links each model cell to the corresponding topographic elements, accounting for variation of the radiation index maps. Then, the water equivalent maps may be easily converted to snow cover maps by using suitable threshold values.

3 TOPMELT integration into ICHYMOD

TOPMELT is integrated within a lumped hydrological model (ICHYMOD, Norbiato et al., 2009), which transforms net precipitation into runoff at the outlet of the basin. The model consists of a soil moisture routine and a flow routing routine. Potential evapotranspiration is estimated by using the Hargreaves method (Hargreaves and Samani, 1982).

The soil moisture routine uses a probability distribution to describe the spatial variation of water storage capacity across a basin, accordingly with the Probability Distributed Model (PDM) by Moore (2007). Saturation excess runoff generated over the basin is integrated to give the total direct runoff entering the fast response pathways to the basin outlet, represented by a cascade of two linear reservoirs in series. Runoff from ice melt is transferred to the outlet through two different routes, depending on glacial till imperviousness. Part of the ice meltwater is input to the soil moisture storage, while the remaining fraction flows directly to the outlet as a cascade of two linear reservoirs in series.
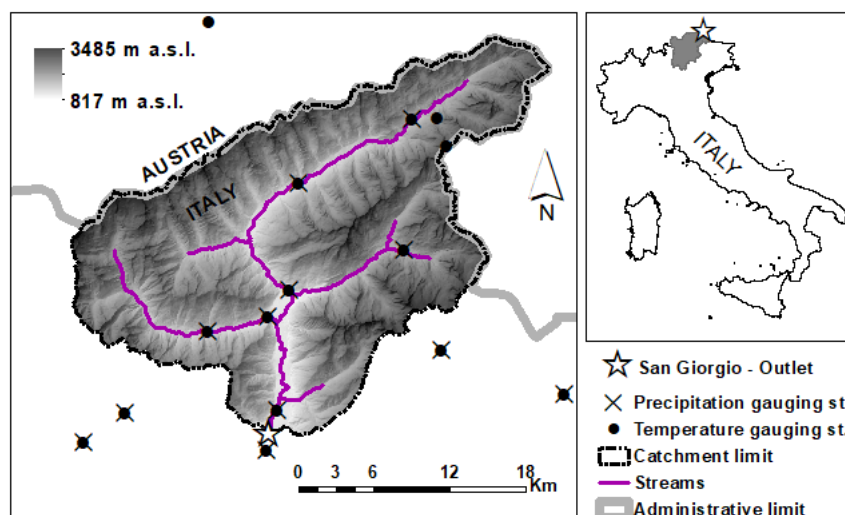
Figure 2. The Aurino river basin closed at S. Giorgio with the position of the hydro-meteorological monitoring stations.

Drainage from the soil enters slow response pathways. The base discharge is routed from groundwater to the catchment outlet through a cubic law storage model. Storage representations of the fast and slow response pathways yield a fast and slow response at the basin outlet which, when summed, gives the total basin flow.

Losses due to evapotranspiration are calculated as a function of potential evapotranspiration and the status of the soil moisture store in the PDM.

4 TOPMELT: Impact of spatial and temporal aggregation scale

4.1 Study site, available data and model set up

TOPMELT is applied in the Aurino river basin closed at San Giorgio, located in the Adige river system in the Easer Alps, Italy (Figure 2). The basin has an extension of 614 km^2, 2.7% of which covered by glaciers for a total of 16.4 km^2. Elevation ranges from 817 to 3485 m a.s.l.. Mean annual basin averaged precipitation is around 950 mm, with values ranging from 850 mm at lower elevations to 1300 mm at the highest elevations. Precipitation and temperature data at hourly time intervals are provided by 15 gauging stations (see Figure 2 for locations), whereas observed discharge are available at the stream-gauge station in S. Giorgio Aurino. The natural runoff regime is partially altered by the reservoir operations over the 25 km^2 Neves basin. Basin topography is described by means of a DTM with a 30 m grid resolution. Satellite observations of snow cover at 250 m resolution are available for the study basin since January 2011 and are provided by an algorithm based on MODIS observations developed by Notarnicola et al. (2013a and 2013b). With this algorithm, MODIS maps provide for each pixel the presence or absence of snow, the presence of clouds, water bodies or pixels with no feature detected. The basin was subdivided

into 14 elevation bands of 200 m each, ranging from 800 to 3600 m above sea level. Elevations bands were then subdivided in a number n_c of radiation classes. To assess the impact of different spatial aggregation levels on model results, five types of class subdivisions of the basin were considered. The elevation bands were divided into n_c=1, 5, 10, 15 and 20 classes, yielding five different spatial aggregation labelled with C1, C5, C10, C15 and C20 respectively. Similarly, to analyse the influence of

5   using different temporal aggregation of the radiation index, five different updating times were used for the computation of the radiation index distribution, with duration of 1, 2, 4, 8 and 12 weeks and labelled W1, W2, W4, W8 and W12 respectively. Variable temporal and spatial discretization allows for different combinations of the space-time aggregation: for example, label W4-C10 refers to a model set up with a temporal aggregation interval of 4 weeks combined with use of 10 radiation classes per elevation band. It is interesting to observe that the model set up W12-C1 resembles a traditional temperature-index model

10   with a radiation correction for elevation band (as in Li and Williams, 2008), whereas the model set-up W1-C20 approximates a fully spatially distributed implementation of the enhanced temperature index model.

4.2   The time integration routine: assessment of pixel transition

An important feature of the model is the use of the time-integration routine to ensure consistency in the snowpack simulation. This routine accounts for pixel transition from one radiation index class to another at the switching time. In this section we

15   analyse the pixel transition, by using an index which represents the percentage of migrating pixels over the total number of pixels belonging to a given elevation band, as follows:

$$MI_i = \frac{\widehat{N}_i}{N_i} \tag{18}$$

where MI_i is the migration index of the transition, N_i is the number of pixels changing class during a switch, and N_i is the number of pixels of the *i-th* elevation band.

20   The percentage of migrating pixels was computed at four elevation bands: the lowest, from the lowest elevation of the basin, 817 m, to 1000 m; two intermediate bands, from 1600 to 1800 m and from 2400 to 2600 m; the highest, from 3400 to 3485 m (which is the max elevation in the basin). The analysis was performed for the five temporal aggregation by using ten radiation index classes, reporting the mean average migration index over the various switches. Results are reported in Figure 3, showing that the percentage of migrating pixels ranges from up to 16% at W1 temporal aggregation to up to 69% at W12

25   temporal aggregation, with a considerable increase of the transition percentage with the increase of temporal aggregation. It is interesting to observe that the transition percentage decreases with increasing the elevation of the band, i.e. with decreasing the spatial dispersion of pixels corresponding to a certain class. One should note that the results are dependent on the number of radiation classes which are used: results (non reported here for the sake of brevity) show that the migration index increases with the number of classes.

30   Finally, a specific analysis aimed to analyse the magnitude of the transition class change. To highlight this aspect, the percentage of pixel which moves by only one class (for example from the second to the third radiation class) was computed and compared to the transition percentage. The percentages were computed and averaged for all the elevation bands. Figure 4 shows this comparison, by considering ten radiation classes, for the five temporal aggregations. For aggregation W12, 42% of
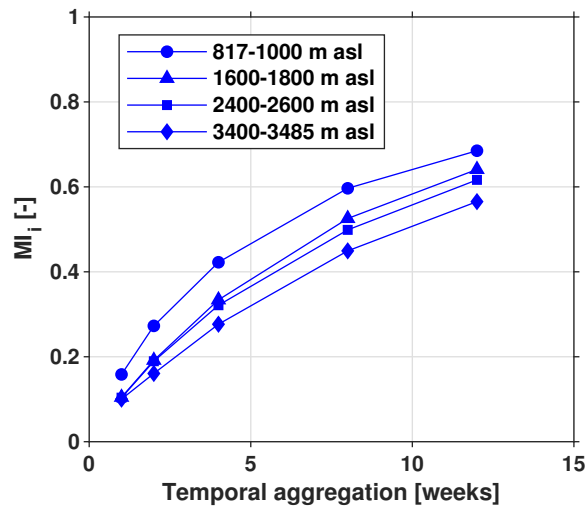
Figure 3. Band migration index for the five temporal aggregations, reported for four elevation bands (lowest elevation band from 817 to 1000 m); from 1600 to 1800 m; from 2400 to 2600 m; highest elevation band from 3400 to 3485 m).
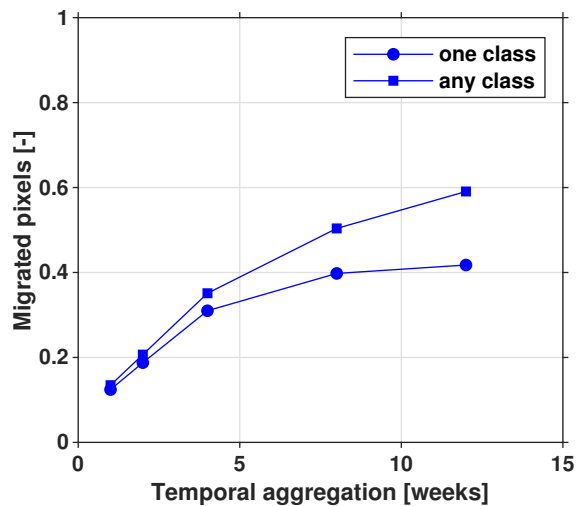

Figure 4. Fraction of migrated pixels computed for the five temporal aggregations over all the elevation bands. Circles refers to pixels that migrated of ±1 energy class, squares to total migrated pixels.

the pixels migrates through one class, 17% through more than one class and only 41% do not migrate at all. For aggregation W1, 12% of the pixels migrates through one class, only 1% through more than one class and 87% of the pixels do not move from the source class at the switch time. These results agree with those reported in Figure 3 and underline the impact of using larger temporal aggregations on the pixel transition between various classes.

4.3 Model calibration and validation

The results reported in Section 4.2 are obviously independent on the specification of the snowpack model parameters; however, their impact on model results (for instance, on the snow water equivalent spatial distribution) depends on the specification of model parameters.

5   TOPMELT and ICHYMOD parameters were identified by means of a two-stage procedure, based on comparison of the simulated outflow with the discharge measured at San Giorgio and on comparison of the simulated snow cover with MODIS data, for the period where MODIS data were available. The model set-up W4-C10 was used for the parameter identification. The following statistics were used for comparing simulated and observed discharges:

$$BIAS = \frac{\sum_{t=1}^{N}(Q_{sim,t} - Q_{obs,t})}{\sum_{t=1}^{N} Q_{obs,t}} \tag{19}$$

10

$$NSE = 1 - \frac{\sum_{t=1}^{N}(Q_{sim,t} - Q_{obs,t})^2}{\sum_{t=1}^{N}(Q_{obs,t} - \bar{Q}_{obs})^2} \tag{20}$$

where $Q_{obs,t}$ and $Q_{sim,t}$ is the observed and simulated discharge at time t, respectively, $\bar{Q}_{obs}$ is the average value of the observed discharges, and N is the number of observations. Optimal values for BIAS and NSE are 0 and 1, respectively.

To compare simulated snow cover (SC) area with MODIS observation, a snow water equivalent threshold was used to declare

15 a snow covered pixel, or conversely a clear one. The threshold was set to 20 mm; it was observed that using lower or higher thresholds within the range 10÷40 mm do not sensibly affect the resulting SC extension. Then, the 30m grids contributing to one MODIS pixel were calculated, and a simulated MODIS-like pixel was considered as snow covered if the percentage of the snow covered 30 m grid size pixels is equal or higher than 50 %. MODIS maps with cloud coverage less than 10% were used for calibration. For analysing the correspondence of simulated versus observed values, the Accuracy Index – ACC skill

20 measure, based on the contingency table, was used:

$$ACC = \frac{TP + TN}{TP + FN + FP + TN} \tag{21}$$

where TP are the number of true positives, i.e. where both model and observation agree on the presence of snow on the pixel; TN is the number of true negatives, FN is the number of false negatives. i.e. pixels which are snow covered according to MODIS and where the model simulates no snow, FP is the number of false positives, i.e. pixels which are free of snow

25 according to MODIS and where the model simulates snow. ACC ranges between 0 and 1 with its optimum at 1. The application of the comparison is exemplified in Figure 5 for May 6, 2011. Following Parajka and Blöschl (2008), the Accuracy Index (Eq. 20) was computed on a pixel base over the 50 cloud-free MODIS maps available within the calibration period from January 1 to June 30, 2011. The resulting spatial distribution of the Accuracy Index is termed Overall Accuracy (OA) map.

The model parameter identification was carried out by using data from October 1, 2001, to September 30, 2012. The period

30 from October 1, 2007 to September 30, 2012 was used for model parameter calibration, with optimisation of the statistics BIAS, NSE and ACC. The period from October 1, 2001 to September 30, 2007 was used for model validation. After parameter
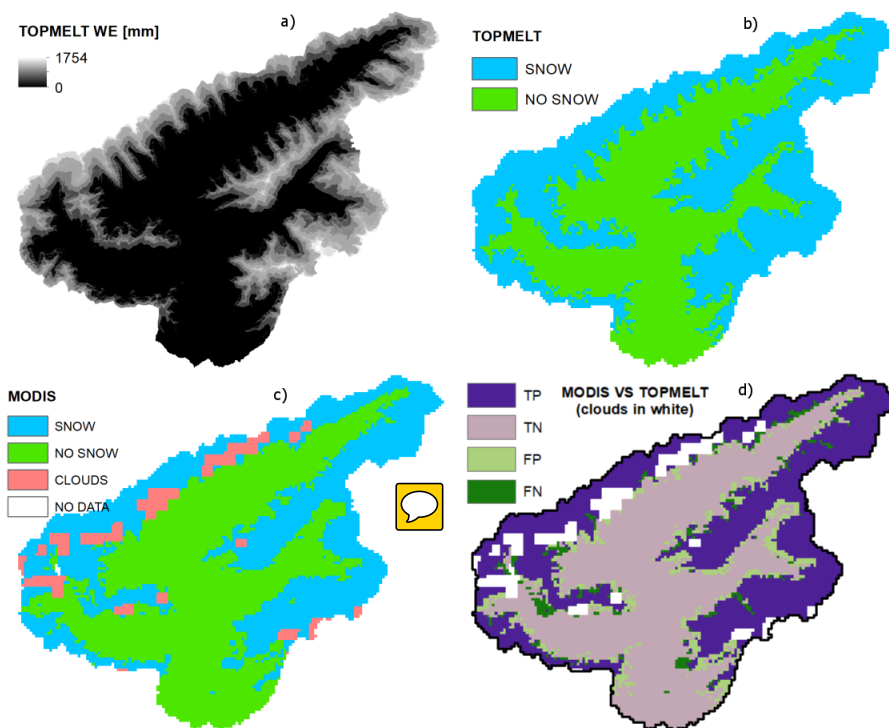
Figure 5. Comparison between simulated and MODIS-derived snow cover map. The comparison is obtained by using the model set up W4-C10 for May 6, 2011.

optimisation, NSE and BIAS values are equal to 0,71 and 2%, respectively, for the calibration period, and to 0,72 and -9%, respectively, for the validation period. A graphical comparison of simulated and observed discharges is reported in Figure 6 for the period May-July 2011, showing the general consistency of the simulation.

The Overall Accuracy map is reported in Figure 7. The figure shows that simulated snow dynamics agreed with MODIS
5 snow cover detection by 71% of the area (OA > 0.7). Lower OA is due to the combined effect of view geometry and forest cover. Forests make MODIS remote sensing of snow challenging because the presence of trees complicates monitoring of snow using remote sensing as trees obscure snow on the ground surface (Notarnicola et al., 2013b). View geometry may be a further major error sources in MODIS snow mapping algorithms in forested areas. This is because the gaps in forest canopies, which are essentially the detectable snow fraction in winter, are lower at off-nadir views (Notarnicola et al., 2013b).

10 **4.4 Impact of temporal and spatial aggregation on model results**

The impact of using different spatial and temporal aggregation on TOPMELT results was carried out by considering the spatial distribution of the water equivalent as a key variable. In this analysis, the finest spatial and temporal discretizations, C20 and W1 respectively, were taken as a reference for the the pixel-by-pixel comparisons. The assessment was carried out at a weekly
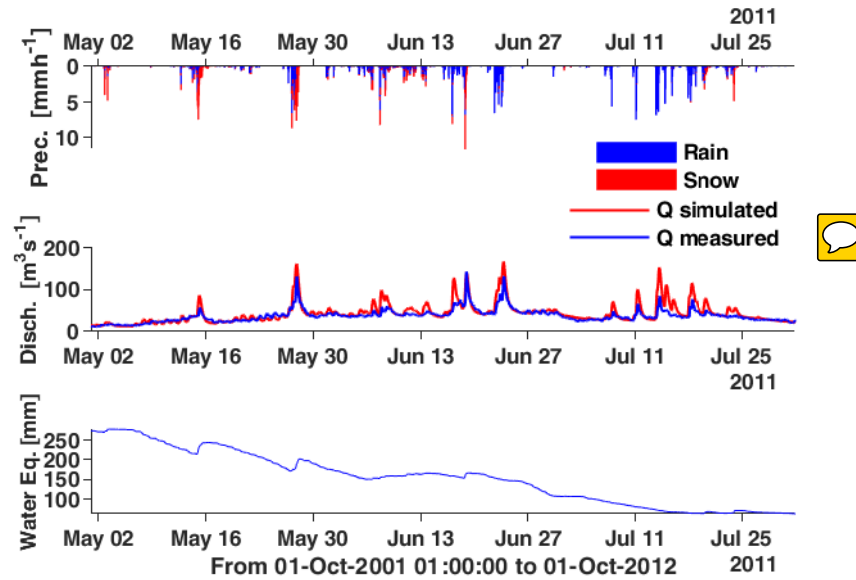
Figure 6. Comparison between simulated (W4-C10) and observed discharge at San Giorgio for the May-July 2011 period.
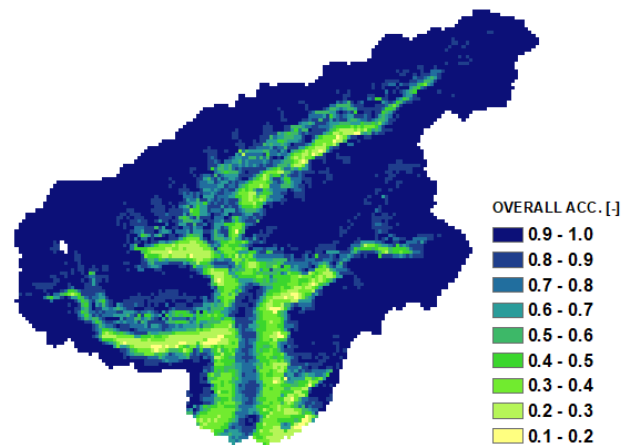

Figure 7. Pixel based overall accuracy (OA) of the comparison between simulated and MODIS-derived snow cover maps, computed from January 1 to June 30, 2011 for a total of 50 MODIS snow cover maps.

time step for the period from October 1, 2010 to June 30, 2011 over 36 maps. This year was selected because MODIS data were available to check the results and the hydrological39 year was an average one.

The NSE statistic (Eq. 20) was used to quantify the agreement bewteen the analysis and reference fields, by excluding from the comparison all the occurrences of zero water equivalent on both maps. One value of the NSE statistic was obtained for each
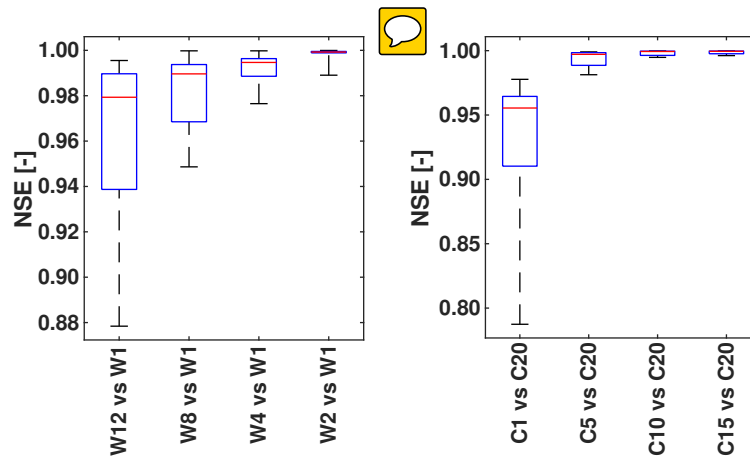
Figure 8. Box plots of NSE computed from the pixel by pixel comparison of the temporal and spatial aggregation series of WE maps, from October 2010 to June 30 2011. On each box, the central mark indicates the median, and the bottom and top edges of the box indicate the 25th and 75th percentiles, respectively. The whiskers extend to the maximum and the minimum efficiency.

of the 36 maps. The intermediate subdivision into radiation classes (C10) was used for the comparison of temporal aggregations W12 to W2 with W1; on the othe hand, the intermediate temporal aggregation of 4 weeks (W4) ws used for the comparison of spatial aggregations C1 to C15 with C20.

The results are reported in Figure 8, where the distributions of the NSE statistics are summarised by using box plots. Figure 7a summarises the results concerning the impact of the temporal aggregation, whereas Figure 7b shows the analysis concerning the spatial aggregation. The impact of using just one radiation class (C1) has a noticeable impact on the results, with NSE ranging from 0,78 to 0,98. Results improve considerably by using 5 classes (C5). The impact of using the longest temporal aggregation (W12) has less worsening impact on the results, with NSE ranging from 0,88 to 0,99. Even in this case, a considerable improvement is obtained by using a reduced temporal aggregation, such as W8. Interestingly, the results resemble the findings obtained by comparing the model set up in terms of pixel migration. The comparison suggests that using the space-time aggregation W4-C10 may provide a good balance between accuracy of the results and computational efficiency.

5 Conclusions

This paper presents TOPMELT, a parsimonious snowpack simulation model which integrates an enhanced temperature index model into a lumped basin scale hydrological model. This is obtained by describing the full spatial distribution of clear sky potential solar radiation by means of a statistical representation, implemented by discretising the area in each elevation band into a number of radiation classes. Snowpack simulation is carried out for each radiation class, rather than for each DTM pixel. When only one radiation class for each elevation band is used, TOPMELT approximates a classical temperature-index model, whereas it approximates a fully distributed model with increasing the number of the radiation. This allows to develop synthesis

in modelling approaches to snow simulation and provides the potential for analysing the impact of spatial and temporal aggregation of radiation fluxes on model results. Furthermore, this approach reduces computational burden, which is a key potential advantage when parameter sensitivity and uncertainty estimation procedures are carried out.

Given the temporal variability of clear sky radiation distribution, the model includes a routine which ensures a consistent

5 temporal simulation of the snow mass balance. The impact of temporal and spatial aggregation of the radiation fluxes on model results is assessed by applying TOPMELT on the 614 km^2 Aurino river basin at S. Giorgio, in the Eastern Italian Alps. The analysis is carried out by examining five temporal aggregation levels (ranging from one to twelve weeks) and five spatial aggregation levels (obtained by subdividing each elevation band into a number of radiation classes ranging from one to twenty), with their impact on the prediction of snow water equivalent distribution. The assessment clearly shows the degradation of

10 model results when using large temporal and spatial aggregation scales, with a model efficiency decreasing up to 20%. On the other hand, .the sensitivity analysis shows that averaging the radiation index over four weeks and using a ten radiation classes subdivision, has a minimal impact on model results.

Future research will examine the scale dependency of the impact of space-time aggregation on TOPMELT-driven runoff simulation, by contrasting small basins (with predominant aspects) and larger basins (where aspects become uncorrelated),

15 and how this may prove relevant for the spatial transferability of enhanced temperature-index model parameters to ungauged basins.

Code availability. TOPMELT is developed in Python, version 3.6, and additionally tested with Python 2.7 (Python Software Foundation, https://www.python.org/). Python installation requires the following additional modules: datetime, inspect, math, os, sys, pyodbc. The code requires the installation of a SQL database (DB) to store input data and to collects output. TOPMELT was developed and tested

20 with MySQL Community Server (GPL), version 5.7.21. TOPMELT source code and a quick user guide are available at the repository http://doi.org/10.5281/zenodo.1342731.

References

Abudu, S., Sheng, Z., Cui, C., Saydi, M., Sabzi, H.-Z. and King, J. P.: Integration of aspect and slope in snowmelt runoff modeling in a mountain watershed, Water Sci. Eng., 9(4), 265–273, doi:10.1016/J.WSE.2016.07.002, 2016.

Anslow, F. S., Hostetler, S., Bidlake, W. R. and Clark, P. U.: Distributed energy balance modeling of South Cascade Glacier, Washington and
5 assessment of model uncertainty, J. Geophys. Res., 113(F2), F02019, doi:10.1029/2007JF000850, 2008.

Armstrong, R. L., Richard L. and Brun, E.: Snow and climate: physical processes, surface energy exchange and modeling, Cambridge University Press., ISBN: 9780521 854542, 2008.

Avanzi, F., De Michele, C., Morin, S., Carmagnola, C. M., Ghezzi, A. and Lejeune, Y.: Model complexity and data requirements in snow hydrology: seeking a balance in practical applications, Hydrol. Process., 30(13), 2106–2118, doi:10.1002/hyp.10782, 2016.

10 Brock, B. W., Willis, I. C. and Sharp, M. J.: Measurement and parameterization of albedo variations at Haut Glacier d'Arolla, Switzerland, J. Glaciol., 46(155), 675–688, doi:10.3189/172756500781832675, 2000.

Carenzo, M., Pellicciotti, F., Rimkus, S. and Burlando, P.: Assessing the transferability and robustness of an enhanced temperature-index glacier-melt model, J. Glaciol., 55(190), 258–274, doi:10.3189/002214309788608804, 2009.

Carturan, L., Cazorzi, F. and Dalla Fontana, G.: Distributed mass-balance modelling on two neighbouring glaciers in Ortles-Cevedale, Italy,
15 from 2004 to 2009, J. Glaciol., 58(209), 467–486, doi:10.3189/2012JoG11J111, 2012.

Cazorzi, F. and Dalla Fontana, G.: Snowmelt modelling by combining air temperature and a distributed radiation index, J. Hydrol., 181(1–4), 169–187, doi:10.1016/0022-1694(95)02913-3, 1996.

Dubayah, R., Dozier, J. and Davis, F. W.: Topographic distribution of clear-sky radiation over the Konza Prairie, Kansas, Water Resour. Res., 26(4), 679–690, doi:10.1029/WR026i004p00679, 1990.

20 Duffie, J. A. and Beckman, W. A.: Solar engineering of thermal processes, Wiley. doi: 10.1016/0038-092X(90)90061-G, 2013.

Essery, R., Morin, S., Lejeune, Y. and B Ménard, C.: A comparison of 1701 snow models using observations from an alpine site, Adv. Water Resour., 55, 131–148, doi:10.1016/J.ADVWATRES.2012.07.013, 2013.

Formetta, G., Kampf, S. K., David, O. and Rigon, R.: Snow water equivalent modeling components in NewAge-JGrass, Geosci. Model Dev., 7(3), 725–736, doi:10.5194/gmd-7-725-2014, 2014.

25 Hargreaves, G.H. and Samani, Z.A.: Estimating potential evapotranspiration. Journal of Irrigation and Drainage Engineering, 108, 223-230, 1982.

Hock, R. and Holmgren, B.: A distributed surface energy-balance model for complex topography and its application to Storglaciären, Sweden, J. Glaciol., 51(172), 25–36, doi:10.3189/172756505781829566, 2005.

Hock, R.: A distributed temperature-index ice- and snowmelt model including potential direct solar radiation, J. Glaciol., 45(149), 101–111,
30 doi:10.1017/S0022143000003087, 1999.

Jóhannesson, T., Sigurdsson, O., Laumann, T. and Kennett, M.: Degree-day glacier mass-balance modelling with applications to glaciers in Iceland, Norway and Greenland, J. Glaciol., 41(138), 345–358, doi:10.3189/S0022143000016221, 1995.

Konz, M. and Seibert, J.: On the value of glacier mass balances for hydrological model calibration, J. Hydrol., 385(1–4), 238–246, doi:10.1016/J.JHYDROL.2010.02.025, 2010.

35 Lee, R.: Forest microclimatology, Columbia University Press. ISBN: 9780231041560, 1978.

Li, X., Williams, M.W: Snowmelt runoff modelling in an arid mountain watershed, Tarim Basin, China. Hydrological Processes, 22(19), 3931-3940, doi:10.1002/hyp.7098, 2008.

Magnusson, J., Wever, N., Essery, R., Helbig, N., Winstral, A. and Jonas, T.: Evaluating snow models with varying process representations for hydrological applications, Water Resour. Res., 51(4), 2707–2723, doi:10.1002/2014WR016498, 2015.

Moore, R. J.: The PDM rainfall-runoff model, Hydrol. Earth Syst. Sci., 11(1), 483–499, doi:10.5194/hess-11-483-2007, 2007.

Norbiato, D., Borga, M., Merz, R., Blöschl, G. and Carton, A.: Controls on event runoff coefficients in the eastern Italian Alps, J. Hydrol., 375(3–4), 312–325, doi:10.1016/J.JHYDROL.2009.06.044, 2009.

Notarnicola, C., Duguay, M., Moelg, N., Schellenberger, T., Tetzlaff, A., Monsorno, R., Costa, A., Steurer, C. and Zebisch, M.: Snow Cover Maps from MODIS Images at 250 m Resolution, Part 1: Algorithm Description, Remote Sens., 5(1), 110–126, doi:10.3390/rs5010110, 2013.

Notarnicola, C., Duguay, M., Moelg, N., Schellenberger, T., Tetzlaff, A., Monsorno, R., Costa, A., Steurer, C. and Zebisch, M.: Snow Cover Maps from MODIS Images at 250 m Resolution, Part 2: Validation, Remote Sens., 5(4), 1568–1587, doi:10.3390/rs5041568, 2013.

Oke, T. R.: Boundary layer climates, Routledge. ISBN: 9780415043199, 1992.

Orgill, J. F. and Hollands, K. G. T.: Correlation equation for hourly diffuse radiation on a horizontal surface, Sol. Energy, 19(4), 357–359, doi:10.1016/0038-092X(77)90006-8, 1977.

Östrem, G.: Ice Melting under a Thin Layer of Moraine, and the Existence of Ice Cores in Moraine Ridges, Geogr. Ann., 41, 228–230, doi:10.2307/4626805, 1959.

Parajka, J., Holko, L., Kostka, Z. and Blöschl, G.: MODIS snow cover mapping accuracy in a small mountain catchment – comparison between open and forest sites, Hydrol. Earth Syst. Sci, 16, 2365–2377, doi:10.5194/hess-16-2365-2012, 2012.

Pellicciotti, F., Brock, B., Strasser, U., Burlando, P., Funk, M. and Corripio, J.: An enhanced temperature-index glacier melt model including the shortwave radiation balance: development and testing for Haut Glacier d'Arolla, Switzerland, J. Glaciol., 51(175), 573–587, doi:10.3189/172756505781829124, 2005.

Ranzi, R. and Rosso, R.: A physically based approach to modelling distributed snowmelt in a small alpine catchment, IAHS Publ. 205: 141-150, 1991.

Swift, L. W.: Algorithm for solar radiation on mountain slopes, Water Resour. Res., 12(1), 108–112, doi:10.1029/WR012i001p00108, 1976.

Tuo, Y., Duan, Z., Disse, M. and Chiogna, G.: Evaluation of precipitation input for SWAT modeling in Alpine catchment: A case study in the Adige river basin (Italy), Sci. Total Environ., 573, 66–82, doi:10.1016/J.SCITOTENV.2016.08.034, 2016.

Vionnet, V., Brun, E., Morin, S., Boone, A., Faroux, S., Le Moigne, P., Martin, E. and Willemet, J.-M.: The detailed snowpack scheme Crocus and its implementation in SURFEX v7.2, Geosci. Model Dev., 5(3), 773–791, doi:10.5194/gmd-5-773-2012, 2012.